LETTER

Perovskite light–emitting diodes based on spontaneously formed submicrometre–scale structures

Yu Cao[1,7], Nana Wang[1,7], He Tian[2,7], Jingshu Guo[3,7], Yingqiang Wei[1], Hong Chen[1], Yanfeng Miao[1], Wei Zou[1], Kang Pan[1], Yarong He[1], Hui Cao[1], You Ke[1], Mengmeng Xu[1], Ying Wang[1], Ming Yang[1], Kai Du[2], Zewu Fu[1], Decheng Kong[1], Daoxin Dai[3], Yizheng Jin[4], Gongqiang Li[1], Hai Li[1], Qiming Peng[1], Jianpu Wang[1]* & Wei Huang[1,5,6]*

Light-emitting diodes (LEDs), which convert electricity to light, are widely used in modern society—for example, in lighting, flat-panel displays, medical devices and many other situations. Generally, the efficiency of LEDs is limited by nonradiative recombination (whereby charge carriers recombine without releasing photons) and light trapping[1–3]. In planar LEDs, such as organic LEDs, around 70 to 80 per cent of the light generated from the emitters is trapped in the device[4,5], leaving considerable opportunity for improvements in efficiency. Many methods, including the use of diffraction gratings, low-index grids and buckling patterns, have been used to extract the light trapped in LEDs[6–9]. However, these methods usually involve complicated fabrication processes and can distort the light-output spectrum and directionality[6,7]. Here we demonstrate efficient and high-brightness electroluminescence from solution-processed perovskites that spontaneously form submicrometre-scale structures, which can efficiently extract light from the device and retain wavelength- and viewing-angle-independent electroluminescence. These perovskites are formed simply by introducing amino-acid additives into the perovskite precursor solutions. Moreover, the additives can effectively passivate perovskite surface defects and reduce nonradiative recombination. Perovskite LEDs with a peak external quantum efficiency of 20.7 per cent (at a current density of 18 milliamperes per square centimetre) and an energy-conversion efficiency of 12 per cent (at a high current density of 100 milliamperes per square centimetre) can be achieved—values that approach those of the best-performing organic LEDs.

Organometal halide perovskites are promising light-emitting materials for solution-processed LED applications because of their high photoluminescence quantum efficiency (PLQE), good charge mobility and excellent colour purity[10–12]. In order to achieve high-efficiency perovskite LEDs, extensive efforts have been made to reduce the nonradiative recombination and improve the PLQE[13–15]. So far, the PLQE of perovskite film has reached as much as 70%, but the peak external quantum efficiency (EQE) of the device electroluminescence is still less than 15%[15–17]. Studies of device physics have shown that, in principle, charge balance is not a limiting factor for the perovskite LED[17]. Therefore, the main loss of efficiency must be due to light trapping—a general efficiency-limiting factor in most types of LEDs. In perovskite LEDs, light trapping could be more serious than in organic LEDs, because the refractive index of perovskites is much higher than those of organic materials[18].

Here we demonstrate effective extraction of trapped light from perovskite LEDs by a spontaneously formed perovskite submicrometre-scale structure. The fabrication process is shown schematically in Fig. 1a. A precursor solution of 5-aminovaleric acid (5AVA), formamidinium iodide (FAI) and PbI_2 with a molar ratio of 0.7/2.4/1 dissolved in N,N-dimethylformamide (DMF; 7 wt.%) was used to deposit perovskite films, which were annealed at 100 °C for 16 min (see Methods for details) before depositing the top charge-transport layer. The device structure is indium tin oxide (ITO)/polyethylenimine ethoxylated (PEIE)-modified zinc oxide (ZnO; thickness 30 nm)/ perovskite (around 50 nm)/poly(9,9-dioctyl-fluorene-co-N-(4-butylphenyl)diphenylamine) (TFB; 40 nm)/molybdenum oxide (MoO_x; 7 nm)/gold (Au; 60 nm). A cross-sectional scanning transmission electron microscope (STEM) image (Fig. 1b) shows the formation of discrete submicrometre-structured perovskites in the emitting layer. Scanning electron microscope (SEM) observations (Fig. 1c) further show that the perovskites are faceted platelets with roughly rectangular shapes. The platelets are randomly tiled on the substrate, and the size of the platelets is between 100 nm and 500 nm. Optical microscope, SEM and atomic force microscopy (AFM) images of different magnifications show that the submicrometre structure is homogeneously distributed on the whole substrate (Extended Data Fig. 1). We note that the perovskite submicron platelets are formed directly through spin-coating the precursor solution, unlike in widely reported methods where organic ligands are used to synthesize perovskite nanocrystals[19,20].

High-angle annular dark-field (HAADF)-STEM tomography observations show that the perovskite submicrometre platelets are embedded in a roughly 8-nm-thick organic layer. In order to avoid possible interference of the TFB layer during the STEM measurement, we prepared a sample by depositing a gold layer directly on top of the ZnO-PEIE/ perovskite. A cross-section STEM tomography reconstruction from a series of images of a tilted sample (Fig. 1d) shows a single layer of perovskite submicrometre platelets distributed on top of the ZnO-PEIE layer, consistent with Fig. 1b. Figure 1e is a STEM tomography image at higher magnification. The contrast seen in this image suggests the existence of a thin layer in which atoms of low atomic number fill in the gaps between the perovskite platelets. Associated energy-dispersive X-ray spectroscopy (EDS) measurements show that carbon, but not lead, has accumulated in the thin layer (which is around 8 nm thick) (Fig. 1f, g). Therefore, we can conclude that there is a thin organic layer filling in the gaps between the perovskite platelets, and that no organic layer can be observed underneath or above the perovskite submicrometre platelets (Fig. 1e–g).

We next investigated how this submicrometre-scale structure is formed. After the 5AVA-perovskite precursor solution has been

[1]Key Laboratory of Flexible Electronics (KLOFE) and Institute of Advanced Materials (IAM), Jiangsu National Synergetic Innovation Center for Advanced Materials (SICAM), Nanjing Tech University (NanjingTech), Nanjing, China. [2]Center of Electron Microscope, State Key Laboratory of Silicon Material, School of Material Science and Engineering, Zhejiang University, Hangzhou, China. [3]Centre for Optical and Electromagnetic Research, State Key Laboratory for Modern Optical Instrumentation, Zhejiang Provincial Key Laboratory for Sensing Technologies, Zhejiang University, Hangzhou, China. [4]Center for Chemistry of High-Performance and Novel Materials, State Key Laboratory of Silicon Materials, and Department of Chemistry, Zhejiang University, Hangzhou, China. [5]Key Laboratory for Organic Electronics and Information Displays, Institute of Advanced Materials, Nanjing University of Posts and Telecommunications, Nanjing, China. [6]Shaanxi Institute of Flexible Electronics (SIFE), Northwestern Polytechnical University (NPU), Xi'an, China. [7]These authors contributed equally: Yu Cao, Nana Wang, He Tian, Jingshu Guo. *e-mail: iamjpwang@njtech.edu.cn; iamwhuang@nwpu.edu.cn
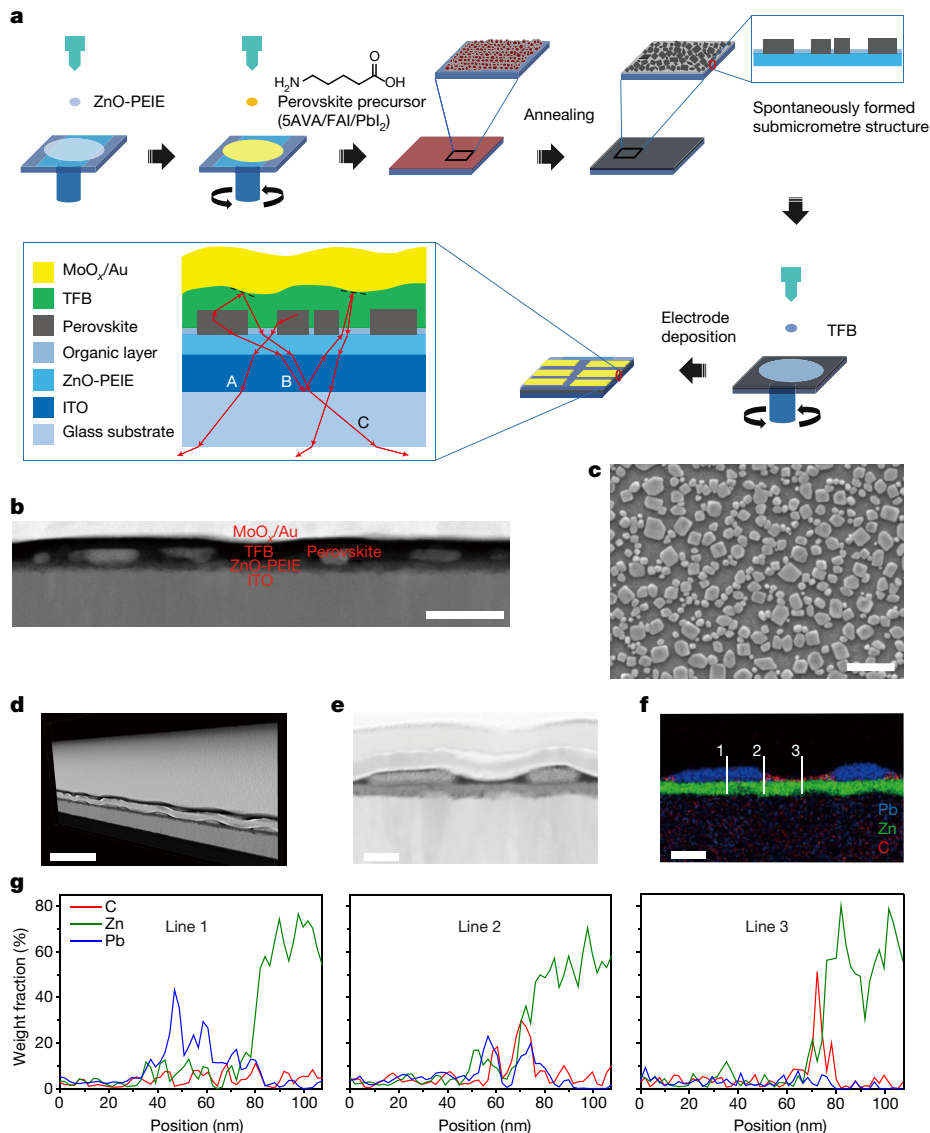
Fig. 1 | Device fabrication and formation of submicrometre structure. a, Fabrication of the device and formation of submicrometre structure. Rays A, B and C, which represent light trapped in devices with a continuous emitting layer, can be extracted by the submicrometre structure. **b**, STEM image of the fabricated device. The scale bar represents 200 nm. **c**, SEM image of the perovskite. The scale bar represents 1 μm. **d**, Tomographic slice of the HAADF-STEM reconstruction of a sample with the structure ITO/ZnO-PEIE/perovskite/Au. The scale bar represents 500 nm. **e**, Cross-section HAADF-STEM tomography image at high magnification. The scale bar represents 100 nm. **f**, Corresponding EDS composite map. The scale bar represents 100 nm. **g**, EDS profiles of carbon, zinc and lead derived from the lines indicated in **f**.

spin-coated onto the ZnO-PEIE substrate, X-ray diffraction (XRD) measurements show the formation of α-phase crystalline FAPbI$_3$ perovskite (Extended Data Fig. 2). By using Scherrer's equation, we can estimate the size of crystallites to be around 40 nm, which is consistent with the SEM observations (Extended Data Fig. 2). Upon annealing, the perovskite crystallites grow and become submicrometre-sized platelets. Meanwhile, the temporal evolution of grazing-angle reflectance Fourier transform infrared spectroscopy (FTIR) spectra (Extended Data Fig. 3) shows that the O–H stretching vibration of 5AVA decreases while the peaks of amide I and amide II become evident as the annealing time increases. This result suggests that 5AVA undergoes a dehydration reaction on top of the ZnO-PEIE, leading to the formation of an organic layer between the perovskite submicrometre platelets. We believe that the thin organic insulating layer resulting from the dehydration reaction of 5AVA can prevent LED leakage currents caused by low coverage of the perovskite layer[21].

The concave–convex structure formed by high-index perovskite and low-index organics (together with the subsequently deposited TFB layer) can extract wide-angle light trapped in the waveguide modes, which is often achieved by embedding insulating grids within the organic layers in organic LEDs[8]. As shown in the enlarged view in Fig. 1a, the wide-angle light (ray A) can enter the low-index organic layer and propagate into the glass substrate. Moreover, the formed perovskite submicrometre platelets have a flat top surface and a relatively uniform height distribution, as confirmed by STEM tomography (Fig. 1d) and AFM measurements (Fig. 2). We emphasize that the discrete perovskite platelets can greatly affect the morphology of the subsequently deposited films. The TFB layer has similar spontaneously formed submicrometre structures, which further carry over to the MoO$_x$/Au electrode, resulting in a corrugated metal thin film with a depth of about 30 nm (Fig. 2). These randomly distributed submicrometre structures can extract light from the waveguide mode in all directions (indicated by rays B and C in Fig. 1a), and will not introduce any spectrum shift and angular dependence.

To verify the quality of perovskite films with this unique submicrometre structure, we measured their optical properties. The absorption and photoluminescence spectra (Fig. 3a) show features typical of three-dimensional (3D) FAPbI$_3$, with absorption until 830 nm
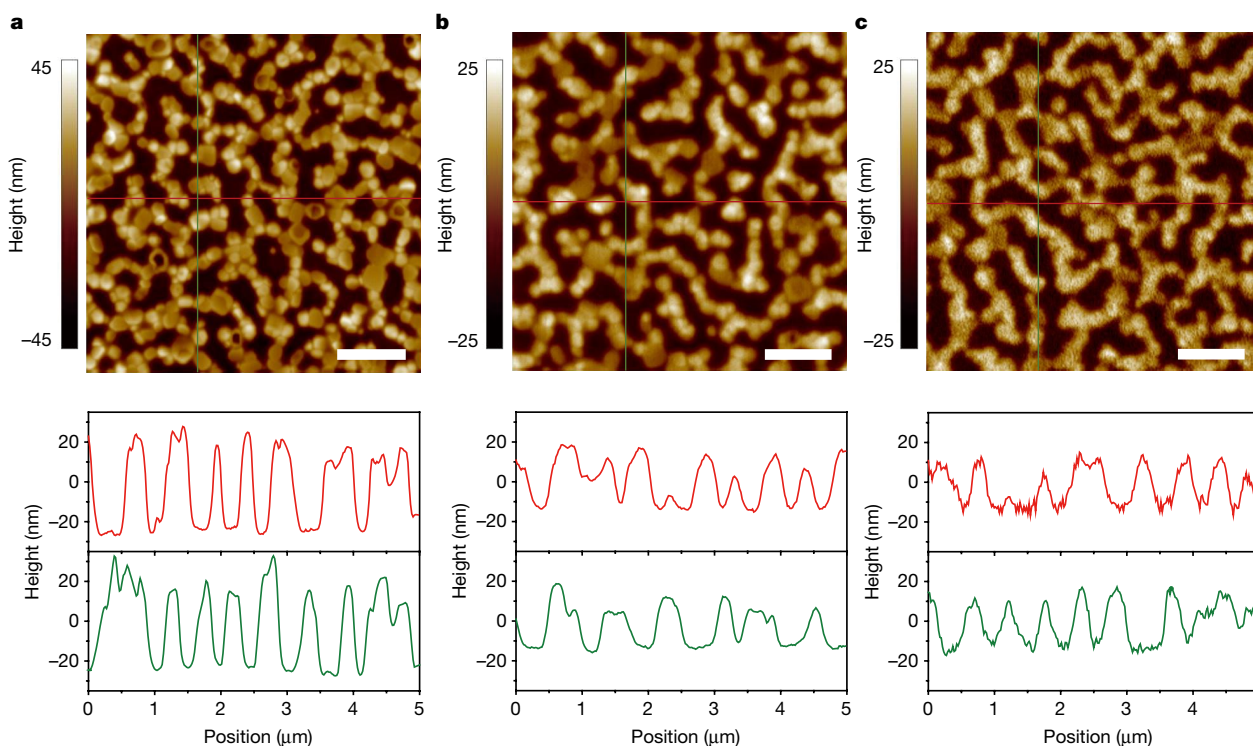
Fig. 2 | AFM height images and multiple line scans. The scale bar represents 1 μm. **a**, ZnO-PEIE/perovskite. The perovskite submicrometre platelets have a height of around 40–50 nm. **b**, ZnO-PEIE/perovskite/TFB. This structure duplicates the morphology of perovskite submicrometre platelets shown in **a**. **c**, ZnO-PEIE/perovskite/TFB/MoO$_x$/Au. This structure also duplicates the morphology of the perovskite layer.

and a photoluminescence peak at 800 nm[13]. The photoluminescence spectrum has a line width of 75 meV, which is much narrower than those of reported FAPbI$_3$ films[13,22], indicating a highly ordered structure in our perovskites. XRD data (Fig. 3b) show that the film has good crystallinity with peaks at around 14°, 28°, 42° and 56°, corresponding to the (111), (222), (333) and (444) crystal planes, respectively, of α-phase FAPbI$_3$ (ref. [23]). The sharp and strong diffraction peaks suggest that the perovskite submicrometre platelets are highly oriented in the direction perpendicular to the substrate, which is consistent with the SEM measurements (Fig. 1c). The perovskite film has a high PLQE of up to about 70% (Fig. 3c), and the PLQE is maintained at a high level of more than 50% at an excitation intensity as low as 0.1 mW cm^{-2}. The results of PLQE measurements suggest that trap-assisted nonradiative recombination—which is a general limiting

factor in 3D perovskites[10,12]—is not substantial in our perovskite platelets. Low trap-assisted nonradiative recombination is confirmed by transient photoluminescence decay measurements, which show a very long photoluminescence lifetime (of about 6 μs) at a low carrier density of 3.4×10^{13} cm^{-3} (Fig. 3d). Transient photoluminescence measurements under various excitation intensities show that a transition from trap-assisted recombination to bimolecular recombination occurs at a carrier density of about 10^{13} cm^{-3}. By fitting the data using a generic kinetic model (Fig. 3d)[24], we can obtain a trap density of 1.5×10^{13} cm^{-3}. Notably, this value is more than one order of magnitude lower than that of previously reported FAPbI$_3$ perovskite films (more than 9×10^{14} cm^{-3})[25]. Extended Data Fig. 4 shows that, without 5AVA in the precursor solution, irregular perovskite clusters are formed with poor crystallinity, strong trap-assisted recombination and very low
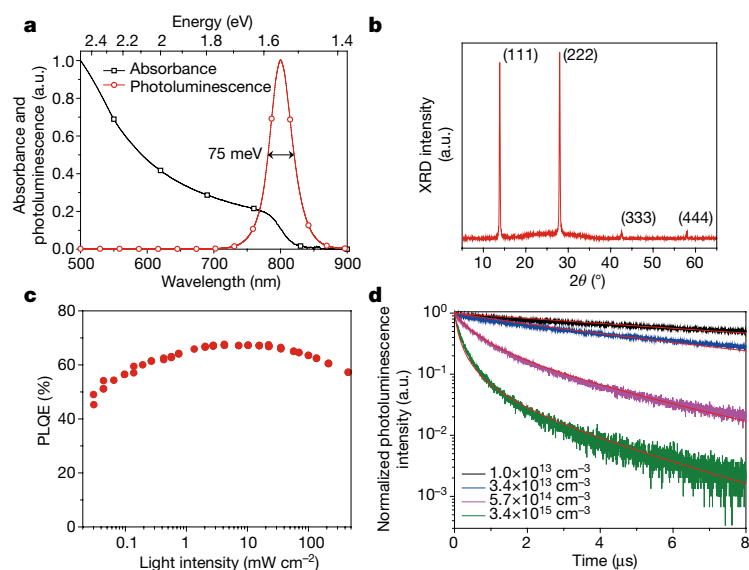

Fig. 3 | Properties of submicrometre-structured perovskite films. a, Absorption and photoluminescence spectra of our perovskite on a ZnO-PEIE substrate. **b**, XRD data from the perovskite films show features of α-phase FAPbI$_3$ with good crystallinity, highly oriented in the perpendicular direction. **c**, Excitation-intensity-dependent PLQE results show a high PLQE of up to 70%; the PLQE is greater than 50% even when the excitation energy is as low as 0.1 mW cm^{-2}, suggesting low trap-assisted nonradiative recombination. **d**, Time-resolved photoluminescence decay transients of submicrometre-structured perovskite under different excitation intensities. Solid lines are fits from the generic kinetic model[24], and a low trap density of 1.5×10^{13} cm^{-3} can be obtained.
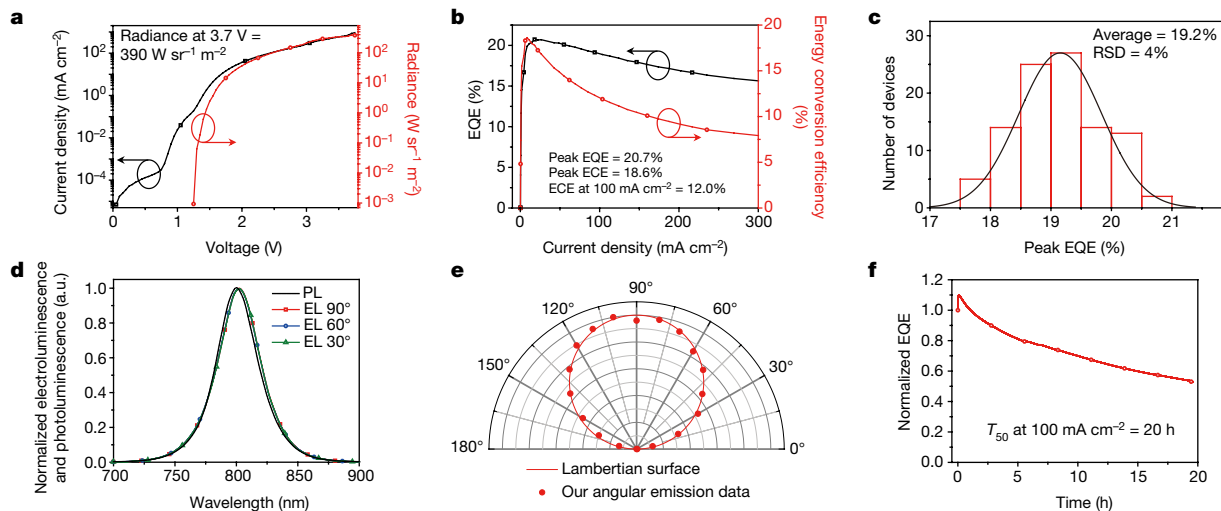
Fig. 4 | Optoelectronic characteristics of our perovskite LEDs.
a, Dependence of current density and radiance on the voltage. **b**, EQE and
ECE plotted against current density. A peak EQE of 20.7% was achieved
under a current density of 18 mA cm^{-2}. **c**, Histogram of peak EQEs.
Statistics from 100 devices show an average peak EQE of 19.2% with a
relative standard deviation (RSD) of 4%. **d**, Photoluminescence (PL) and
electroluminescence (EL) spectra of the device at different viewing angles.
e, The angular distribution of the radiation intensity follows a Lambertian
profile. **f**, Stability of the device measured at a constant current density of
100 mA cm^{-2}.

PLQEs at low excitation intensities. These findings indicate that 5AVA
has the important role of passivating surface defects and enhancing
the emission properties of perovskites. We note that a similar effect has
previously been observed[26–29].

These analyses suggest that our submicrometre-scale crystalline per-
ovskites have great potential for realizing high-efficiency LED devices.
The current-density/radiance/voltage characteristics of LEDs based
on the structured perovskites are shown in Fig. 4a. Owing to the good
charge mobility of 3D perovskites (in comparison with organic emit-
ters) and efficient charge injection, the current density and radiance
increase quickly once the device turns on at 1.25 V, yielding a high
brightness of up to 390 W sr^{-1} m^{-2} at a low voltage of 3.7 V. The device
current is low before the electroluminescence turns on, indicating that
the leakage current is not important in our LED devices, and further
suggesting that the insulator layer between the perovskite submicro-
metre platelets is pinhole free. The peak EQE reaches 20.7% at a current
density of 18 mA cm^{-2} (Fig. 4b), representing a record efficiency for
perovskite LEDs. The brightness at the peak EQE is 18.4 W sr^{-1} m^{-2}
(corresponding to a photon flux of 2.33×10^{20} m^{-2} s^{-1}), which is
at least one order of magnitude higher than that of state-of-the-art
organic LEDs (Extended Data Table 1). Owing to the low operation
voltage and low EQE roll-off, the peak energy conversion efficiency
(ECE, or wall–plug efficiency) reaches 18.6% at a current density of
around 10 mA cm^{-2} and is maintained at 12.0% at a high current
density of 100 mA cm^{-2}. Notably, the ECE at the current density of
100 mA cm^{-2} is much higher than that of the best-performing organic
LEDs (Extended Data Table 1). An EQE histogram for 100 devices
shows an average EQE of 19.2%, with a low relative standard deviation
of 4% (Fig. 4c), indicating that the device performance is highly repro-
ducible. The electroluminescence peak is located at 803 nm, consistent
with the photoluminescence emission peak. The electroluminescence
spectra do not vary at different viewing angles (Fig. 4d), and the angu-
lar emission intensity of our perovskite LEDs follows a Lambertian
profile (Fig. 4e). These findings indicate that the randomly distrib-
uted submicrometre structure does not introduce a periodic grating
effect. In addition, devices with a simple glass-epoxy encapsulation
exhibit a half-lifetime (T_{50}, defined as the time taken for the EQE to
drop to half of its initial value) of 20 h at the high constant current
density of 100 mA cm^{-2} (Fig. 4f). This good stability can be attributed
partially to the passivation effect of 5AVA, which can result in similar
stability-enhancement effects in perovskite solar cells[26,27]. Moreover,
we believe that the high ECE is beneficial to the perovskite stability,
because less thermal energy is generated. We note that the T_{50} of 20 h
at 100 mA cm^{-2} is also comparable with those of state-of-the-art near-
infrared organic LEDs[30].

Considering that the PLQE of the perovskite layer is 70%, we
suggest that the remarkable EQE of the electroluminescence is largely
due to the enhanced light outcoupling efficiency of the spontaneously
formed submicrometre structures shown in Figs. 1 and 2. To evalu-
ate the enhancement factor of light outcoupling, we performed 3D
finite-difference-time-domain (3D-FDTD) simulations (see Methods
for details). The results show that a reference device with a continuous
and flat emitting layer has an outcoupling efficiency of 21.8%. The out-
coupling efficiency of a device with submicrometre structures reaches
about 30% (Extended Data Fig. 5), which is consistent with the high
EQE obtained in our devices. We also characterized our LED device
under low temperatures, where the nonradiative recombination can be
suppressed as the trap states are frozen out[24]. In this case, we can assume
that the internal quantum efficiency of the LED device reaches nearly
100%, and the measured EQE is the outcoupling efficiency of the LED
devices. Extended Data Fig. 6 shows that the device EQE increases with
decreasing temperature and reaches 30% at 6 K, which is consistent
with our 3D-FDTD simulation results.

We highlight that the device performance depends on several pro-
cessing conditions, such as the ratio of 5AVA to FAI and PbI$_2$ (Extended
Data Fig. 4) and the concentration of the precursor solution (Extended
Data Figs. 7, 8). As discussed above, the PLQEs of the perovskite films
can be improved by adding 5AVA into the precursor solutions. The
formation of the submicrometre structure can also be affected by the
ratio of 5AVA and the concentration of the precursor solution. After
adding 5AVA, faceted perovskite platelets with submicrometre struc-
ture gradually form (Extended Data Fig. 4). Meanwhile, the PLQE and
photoluminescence lifetime are greatly improved owing to a reduced
defect density, leading to enhanced device efficiency (Extended Data
Fig. 4). With more concentrated precursor solutions, there is a tendency
to form larger crystallites as well as thicker and higher-surface-coverage
films, which can greatly affect the leakage current, turn-on voltage,
radiance and light outcoupling (Extended Data Fig. 7). When a solution
of lower concentration is used, the devices show larger leakage current
and lower EQEs. With thicker perovskite films, the devices become
less conductive, which increases the turn-on voltage and reduces the
brightness. Our current-processing parameters represent optimized
conditions, which lead to perovskite films with a combination of high
PLQE, low leakage current and preferred submicrometre structures.

We think that the PLQE and outcoupling efficiency could be enhanced further by using more effective additives to suppress the nonradiative recombination, and more optimized processing to control the sub-micrometre structure. Interestingly, conventional 3D perovskites are usually very sensitive to the fabrication process, but our device can maintain an average peak EQE of more than 18% with an annealing time of between 14 min and 20 min (Extended Data Fig. 2), showing that this solution-processing protocol has a relatively wide processing window.

We have also found that adding amino acids into the precursor solution is a general strategy for growing high-quality $FAPbI_3$ per-ovskites with submicrometre structure. Amino acids of different chain lengths—6-aminocaproic acid (6ACA) and 7-aminoheptanoic acid (7AHA)—have similar effects to 5AVA in achieving high-efficiency perovskite LEDs (Extended Data Fig. 9). After 6ACA or 7AHA is added to the precursor solution, the resulting films have morphologies and PLQEs analogous to those of films containing 5AVA. Without extensive optimization, the LEDs processed from precursor solutions with 6ACA or 7AHA also exhibit good peak EQEs of 18.2% and 17.3%, respectively.

It has been demonstrated that the EQEs of planar-type LEDs can be enhanced by improving the light outcoupling. However, tradition-ally this requires complex fabrication processes, and it is difficult to maintain a consistent emission spectrum at different viewing angles. Remarkably, these limitations can be avoided in perovskite LEDs by using the simple strategy described here, at little extra cost of fabri-cation. The resulting peak EQE of our perovskite LED approaches those of the best-performing organic LEDs. In contrast to LEDs based on group III–V semiconductors, in organic LEDs processed at low temperatures it is difficult to maintain high ECEs at high current densities, owing to their excitonic nature and low charge mobilities[1]. But low-temperature solution-processed perovskite LEDs demonstrate remarkably high ECEs at high current densities, suggesting the unique possibility of achieving large planar LEDs with high efficiency at high brightness.

Online content

Any methods, additional references, Nature Research reporting summaries, source data, statements of data availability and associated accession codes are available at https://doi.org/10.1038/s41586-018-0576-2.

1. Lee, J. et al. Deep blue phosphorescent organic light-emitting diodes with very high brightness and efficiency. *Nat. Mater.* **15**, 92–98 (2016).
2. Dai, X. et al. Solution-processed, high-performance light-emitting diodes based on quantum dots. *Nature* **515**, 96–99 (2014).
3. Waltereit, P. et al. Nitride semiconductors free of electrostatic fields for efficient white light-emitting diodes. *Nature* **406**, 865–868 (2000).
4. Lee, Y.-J. et al. A high-extraction-efficiency nanopatterned organic light-emitting diode. *Appl. Phys. Lett.* **82**, 3779–3781 (2003).
5. Bulović, V. et al. Weak microcavity effects in organic light-emitting devices. *Phys. Rev. B* **58**, 3730–3740 (1998).
6. Matterson, B. J. et al. Increased efficiency and controlled light output from a microstructured light-emitting diode. *Adv. Mater.* **13**, 123–127 (2001).
7. Ziebarth, J. M., Saafir, A. K., Fan, S. & McGehee, M. D. Extracting light from polymer light-emitting diodes using stamped bragg gratings. *Adv. Funct. Mater.* **14**, 451–456 (2004).
8. Sun, Y. & Forrest, S. R. Enhanced light out-coupling of organic light-emitting devices using embedded low-index grids. *Nat. Photon.* **2**, 483–487 (2008).
9. Koo, W. H. et al. Light extraction from organic light-emitting diodes enhanced by spontaneously formed buckles. *Nat. Photon.* **4**, 222–226 (2010).
10. Deschler, F. et al. High photoluminescence efficiency and optically pumped lasing in solution-processed mixed halide perovskite semiconductors. *J. Phys. Chem. Lett.* **5**, 1421–1426 (2014).
11. Tan, Z.-K. et al. Bright light-emitting diodes based on organometal halide perovskite. *Nat. Nanotechnol.* **9**, 687–692 (2014).
12. Wang, J. et al. Interfacial control toward efficient and low-voltage perovskite light-emitting diodes. *Adv. Mater.* **27**, 2311–2316 (2015).
13. Wang, N. et al. Perovskite light-emitting diodes based on solution-processed self-organized multiple quantum wells. *Nat. Photon.* **10**, 699–704 (2016).
14. Yuan, M. et al. Perovskite energy funnels for efficient light-emitting diodes. *Nat. Nanotechnol.* **11**, 872–877 (2016).
15. Yang, X. et al. Efficient green light-emitting diodes based on quasi-two-dimensional composition and phase engineered perovskite with surface passivation. *Nat. Commun.* **9**, 570; correction **9**, 1169 (2018).
16. Sun, Y. et al. The formation of perovskite multiple quantum well structures for high performance light-emitting diodes. *npj Flex. Electron.* **2**, 12 (2018).
17. Zou, W. et al. Minimising efficiency roll-off in high-brightness perovskite light-emitting diodes. *Nat. Commun.* **9**, 608 (2018).
18. Richter, J. M. et al. Enhancing photoluminescence yields in lead halide perovskites by photon recycling and light out-coupling. *Nat. Commun.* **7**, 13941 (2016).
19. Schmidt, L. C. et al. Nontemplate synthesis of $CH_3NH_3PbBr_3$ perovskite nanoparticles. *J. Am. Chem. Soc.* **136**, 850–853 (2014).
20. Sichert, J. A. et al. Quantum size effect in organometal halide perovskite nanoplatelets. *Nano Lett.* **15**, 6521–6527 (2015).
21. Lin, X. et al. Electrically-driven single-photon sources based on colloidal quantum dots with near-optimal antibunching at room temperature. *Nat. Commun.* **8**, 1132 (2017).
22. Fu, Y. et al. Stabilization of the metastable lead iodide perovskite phase via surface functionalization. *Nano Lett.* **17**, 4405–4414 (2017).
23. Pang, S. et al. $NH_2CH=NH_2PbI_3$: an alternative organolead iodide perovskite sensitizer for mesoscopic solar cells. *Chem. Mater.* **26**, 1485–1491 (2014).
24. Stranks, S. D. et al. Recombination kinetics in organic-inorganic perovskites: excitons, free charge, and subgap states. *Phys. Rev. Appl.* **2**, 034007 (2014).
25. Gélvez-Rueda, M. C., Renaud, N. & Grozema, F. C. Temperature dependent charge carrier dynamics in formamidinium lead iodide perovskite. *J. Phys. Chem. C* **121**, 23392–23397 (2017).
26. Mei, A. et al. A hole-conductor-free, fully printable mesoscopic perovskite solar cell with high stability. *Science* **345**, 295–298 (2014).
27. Zhang, T. et al. In situ fabrication of highly luminescent bifunctional amino acid crosslinked 2D/3D $NH_3C_4H_9COO(CH_3NH_3PbBr_3)_n$ perovskite films. *Adv. Funct. Mater.* **27**, 1603568 (2017).
28. de Quilettes, D. W. et al. Impact of microstructure on local carrier lifetime in perovskite solar cells. *Science* **348**, 683–686 (2015).
29. Lee, S. et al. Amine-based passivating materials for enhanced optical properties and performance of organic-inorganic perovskites in light-emitting diodes. *J. Phys. Chem. Lett.* **8**, 1784–1792 (2017).
30. Sassi, M. et al. Near-infrared roll-off-free electroluminescence from highly stable diketopyrrolopyrrole light emitting diodes. *Sci. Rep.* **6**, 34096 (2016).

Author contributions J.W. had the idea for and designed the experiments. J.W. and W.H. supervised the work. Y.C. carried out device fabrication and characterizations, with the assistance of Y.M., H.Cao and Y.K.; Y.C., W.Z., M.X., Y.Wang, Z.F., D.K., Q.P., M.Y. and Y.H. conducted the optical measurements. Y.Wei and H.L. carried out AFM measurements. H.Chen, G.L. and Y.J. carried out FTIR characterizations. H.T. carried out high-resolution TEM and STEM characterizations with the assistance of Y.C., Y.Wei and K.D.; J.G. carried out optical simulations of the device with the assistance of K.P.; D.D. supervised the optical simulation. J.W., N.W. and Y.C. analysed the data. N.W. wrote the first draft of the manuscript and J.W. and W.H. provided major revisions. All authors discussed the results and commented on the manuscript.

METHODS

Device fabrication. ZnO nanocrystals were spin-coated onto ITO-coated glass substrates, forming the electron-transport layer. Then an ultrathin PEIE layer was fabricated onto the ZnO layer to decrease the work function and improve the wetting property of ZnO[12,13,31]. A precursor perovskite solution was prepared by dissolving 5AVA, FAI and PbI$_2$ with different molar ratios and concentrations in dimethylformamide (DMF), and stirring at 60 °C for 2 h in a nitrogen-filled glovebox. A perovskite precursor containing 6ACA (or 7AHA) was prepared by dissolving 6ACA (or 7AHA), FAI and PbI$_2$ with a molar ratio of 0.7/2.4/1 in DMF. Next, the perovskite films were prepared by spin-coating the precursor solution onto the PEIE-treated ZnO films and annealing them at 100 °C. TFB was spin-coated onto the perovskite film, forming the hole-transport layer. Finally, an MoO$_x$/Au electrode was thermally evaporated through a shadow mask, defining the device area of 3 mm^2.

Device characterization. We tested the perovskite LEDs on top of an integration sphere at room temperature in a nitrogen-filled glovebox, in which only forward light emission can be collected[2,32]. We measured the devices from zero bias to forward bias at a rate of 0.05 V s^{-1}, and recorded the data with the first scan without pre-bias. We carried out low-temperature characterizations of the LEDs in a cryostat (Oxford Instruments NanoScience, OptistatAC-V12W). The stability of the devices was measured in air with simple glass-epoxy encapsulation. We measured the angular dependence of emission intensity and spectra using a Thorlabs PDA100A detector and QE65 Pro spectrometer, respectively. Three sets of perovskite LEDs from the same batch were cross-checked at Nanjing Tech University, the University of Cambridge (Optoelectronics Group) and Zhejiang University (Y. Jin group), and the results are consistent (Extended Data Table 2).

Film characterizations. We collected STEM images of cross-sectional devices on a FEI Titan G2 80-200 ChemiSTEM operated at 200 keV. We used the FEI Talos analytical FEG scanning transmission electron microscope, which includes the Super-X energy-dispersive X-ray spectroscopy (EDS) system with four silicon drift detectors for superior sensitivity and mapping capabilities. We acquired images every 2° in the range −150° to +150° to avoid a missing-wedge effect, with an 80-keV high voltage and 200-pA incident beam current to avoid beam damage. Visualization and reconstruction was done using FEI Inspect 3D and Avizo software. We obtained SEM images of perovskite films with a JEOL5 JSM-7800F SEM. The surface morphology of different layers was collected by AFM (Bruker, Dimension ICON).

We used an ultraviolet/visible spectrophotometer with an integrating sphere (PerkinElmer, Lambda 950) to measure the absorbance spectra. Photoluminescence spectra were measured using a QE65 Pro spectrometer and a 445-nm continuous-wave laser as an excitation source. Time-resolved photoluminescence measurements were performed with an Edinburgh Instruments spectrometer (FLS980), having excited the perovskite films with a 633-nm pulsed laser of various intensities. We measured the PLQE of perovskite films by combining a continuous-wave laser, optical fibre, spectrometer and integrating sphere[33].

We collected XRD data using a Bruker D8 Advance. Grazing-angle FTIR spectra were performed with a Thermo Fisher IS50 equipped with a Smart SAGA reflectance accessory. The samples were prepared on Au-coated quartz substrates.

Simulations. We analysed the spatial frequency spectrum of the randomly distributed perovskite map of a real device by using a two-dimensional fast Fourier transform (FFT). The range P_{range} is given as P_1–P_2, corresponding to the major spatial frequency components. 3D-FDTD (Lumerical Solutions) simulations were carried out for the regular periodic devices with a cycle P ($l_e = P/2$, where l_e is the length of the perovskite platelets) to estimate the outcoupling efficiency, $\eta_{FDTD}(P)$. Then the average value of the calculated efficiency $\eta_{FDTD}(P_1)$, $\eta_{FDTD}(P_1 + 1 \text{ nm})$, ... $\eta_{FDTD}(P_2)$ was used to evaluate the outcoupling efficiency of the real device (with a wideband spatial frequency spectrum). The error corresponds to the standard deviation.

The SEM data were imported and a picture with $N \times N$ pixels was obtained, which was then discretized as the function:

$$f(x, y) = \begin{cases} 1 & (\text{EML area}) \\ 0 & (\text{else area}) \end{cases}$$

where $x, y = a, 2a..., Na$, and a is the pixel size. The spatial frequency spectrum:

$$F(U_x, U_y) = \int_{-\infty}^{\infty} \int_{-\infty}^{\infty} f(x, y) e^{-j2\pi(U_x x + U_y y)} dx dy$$

was obtained by using FFT (Extended Data Fig. 5c). For example, we can obtain a discretized picture with 1,001 × 1,001 pixels and $a = 3.57$ nm (Extended Data Fig. 5b). The major peaks of $|F(U_x, U_y)|$ are found in the range $r_1 \cdot (2\pi/a) \le |U_x|$, $|U_y| \le r_2 \cdot (2\pi/a)$ ($r_1 = 3.52 \times 10^{-3}$ and $r_2 = 9.83 \times 10^{-3}$, as labelled with white squares in Extended Data Fig. 5c). Then P_{range} can be established as 363–1,015 nm ($P_1 = a/r_2$, $P_2 = a/r_1$), resulting in an outcoupling efficiency of 28.7% ± 2.6% when the convex height, h, is 30 nm.

For the 3D-FDTD simulations, we used a window of 7 μm × 7 μm × 0.45 μm, and applied localized refined meshes (Δx, Δy and Δz). We chose $\Delta x = \Delta y = \Delta z = 2$ nm in the dipole source area, and $\Delta z = 1$ nm in the convex structures. In order to simulate the incoherent isotropic light-generation process, we did simulations thrice by choosing different source polarizations for the dipole source. The near field at the glass–ITO interface was then used to calculate the outcoupled far field in air by using Lumerical's far field analysis group, in which the air–glass interface was taken into consideration. We measured the refractive indices of Au, MoO$_x$, TFB, perovskite and ZnO with an ellipsometer (KLA Tencor, P-7), and took the refractive indices of ITO and glass from the literature[34,35]. To obtain the optical constants of perovskite in the simulation, we prepared a continuous FAPbI$_3$ film for the ellipsometer measurement, and fitted the measurement result using the dispersion laws of the Tauc–Lorentz model, the Gauss model and two sets of Lorentz oscillators. We ignored the imaginary part of the refractive index of the perovskite in the simulation. We carried out the simulation at a wavelength of 800 nm. For each periodic device, we used 3 × 3 uniform distributed sources in one perovskite cubic in separate simulations. Dividing the average outcoupling power by the average source power obtained from all the simulations (varying the locations and polarizations of sources), we obtained the theoretical outcoupling efficiency of the device.

Data availability

The data that support the finding of this study are available from the corresponding author upon reasonable request.

31. Zhou, Y. et al. A universal method to produce low-work function electrodes for organic electronics. *Science* **336**, 327–332 (2012).
32. Forrest, S. R., Bradley, D. D. C. & Thompson, M. E. Measuring the efficiency of organic light-emitting devices. *Adv. Mater.* **15**, 1043–1048 (2003).
33. de Mello, J. C., Wittmann, H. F. & Friend, R. H. An improved experimental determination of external photoluminescence quantum efficiency. *Adv. Mater.* **9**, 230–232 (1997).
34. Rubin, M. Optical properties of soda lime silica glasses. *Sol. Energy Mater.* **12**, 275–288 (1985).
35. König, T. A. F. et al. Electrically tunable plasmonic behavior of nanocube–polymer nanomaterials induced by a redox-active electrochromic polymer. *ACS Nano* **8**, 6182–6192 (2014).
36. Ogomi, Y. et al. All-solid perovskite solar cells with HOCO-R-NH$_3^+$I$^-$ anchor-group inserted between porous titania and perovskite. *J. Phys. Chem. C* **118**, 16651–16659 (2014).
37. Tamaddon, F., Aboee, F. & Nasiri, A. ZnO nanofluid as a structure base catalyst for chemoselective amidation of aliphatic carboxylic acids. *Catal. Commun.* **16**, 194–197 (2011).
38. Ly, K. T. et al. Near-infrared organic light-emitting diodes with very high external quantum efficiency and radiance. *Nat. Photon.* **11**, 63–68 (2017).
39. Kim, K.-H. et al. Phosphorescent dye-based supramolecules for high-efficiency organic light-emitting diodes. *Nat. Commun.* **5**, 4769 (2014).
40. Helander, M. G. et al. Chlorinated indium tin oxide electrodes with high work function for organic device compatibility. *Science* **332**, 944–947 (2011).
41. Lin, T.-A. et al. Sky-blue organic light emitting diode with 37% external quantum efficiency using thermally activated delayed fluorescence from spiroacridine-triazine hybrid. *Adv. Mater.* **28**, 6976–6983 (2016).
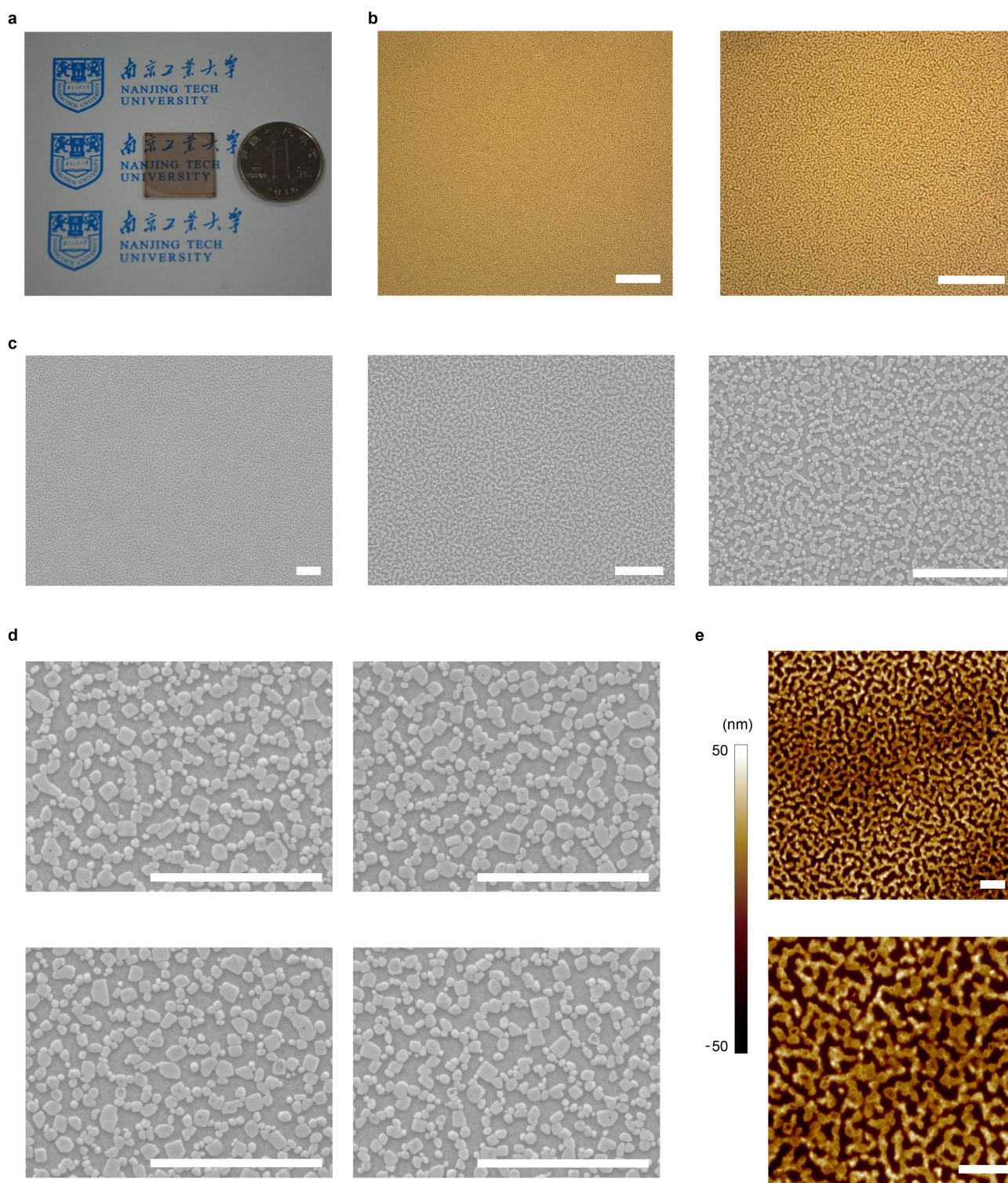
Extended Data Fig. 1 | Images of perovskite films. a, Photograph of a perovskite film on a 2 cm × 2 cm glass/ZnO-PEIE substrate, alongside a coin. The perovskite film is shiny and uniform. **b**, Optical microscope images with different magnifications. The scale bars represent 30 μm. **c**, SEM images with different magnifications. The scale bars represent 3 μm. **d**, High-magnification SEM images of randomly selected regions. The scale bars represent 3 μm. **e**, AFM images with different magnifications. The scale bars represent 2 μm. The images show the submicrometre-scale structure of the perovskite film.
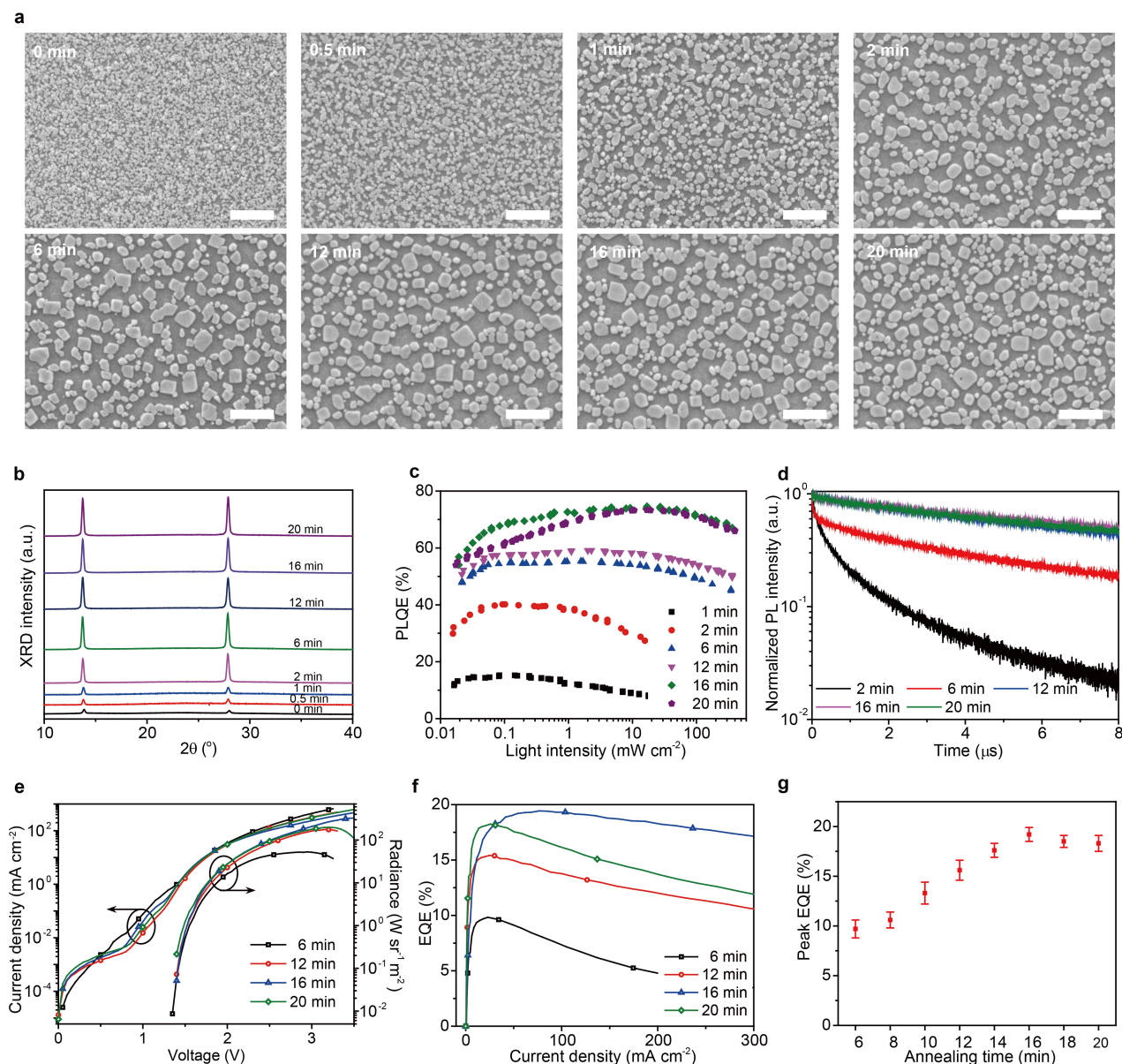
Extended Data Fig. 2 | Characterization of our perovskite films and perovskite LEDs fabricated with different annealing times. a, SEM images of perovskite films. The scale bars represent 1 μm. The images show that as the annealing time increases, the crystallites grow from small particles and become larger and more faceted. When the annealing time is more than 6 min, similar submicrometre-scale structures form. **b**, XRD spectra. Crystallinity is enhanced as the annealing time increases, in agreement with the SEM images. **c**, Excitation-intensity-dependent PLQEs. Trap densities gradually decrease as the annealing time increases, resulting in PLQEs of more than 60% when the annealing time is between 16 and 20 min. **d**, Time-resolved photoluminescence (PL) decay transients (at a carrier density of 1.0×10^{13} cm^{-3}). The films show longer PL decay lifetimes at longer annealing times. **e**, Dependence of current density and radiance on the driving voltage. The circles denote a bunch of curves; the arrows show the *y* axis to which a given bunch belongs. **f**, EQE versus current density. **g**, Peak EQE versus annealing time. An average peak EQE of more than 18% can be maintained with annealing times of between 14 and 20 min. Error bars correspond to the standard deviation.
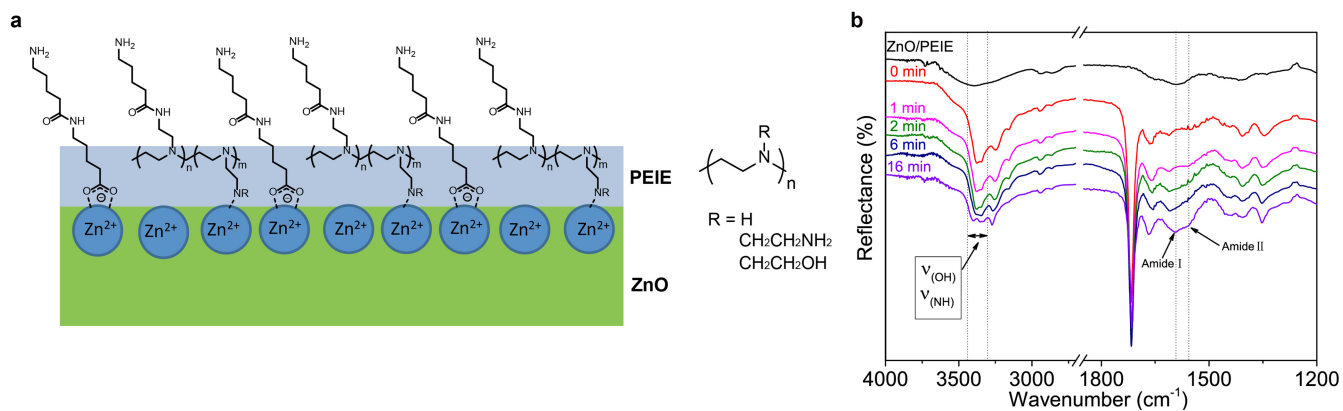
Extended Data Fig. 3 | Formation of the organic layer surrounding the submicrometre structures. a, Dehydration reaction of 5AVA on top of the ZnO-PEIE surface[36,37]. **b**, Grazing-angle reflectance FTIR spectra of perovskite films at various annealing times. As the annealing time increases, the peak at 3,400–3,300 cm^{-1} (ν_{O-H} in 5AVA) decreases; simultaneously, peaks appear at 1,620 cm^{-1} and 1,550 cm^{-1}, which can be assigned as amide I band ($\nu_{C=O}$) and amide II band (δ_{N-H}), respectively. These spectra indicate dehydration reactions of 5AVA, leading to the formation of an organic layer during annealing.
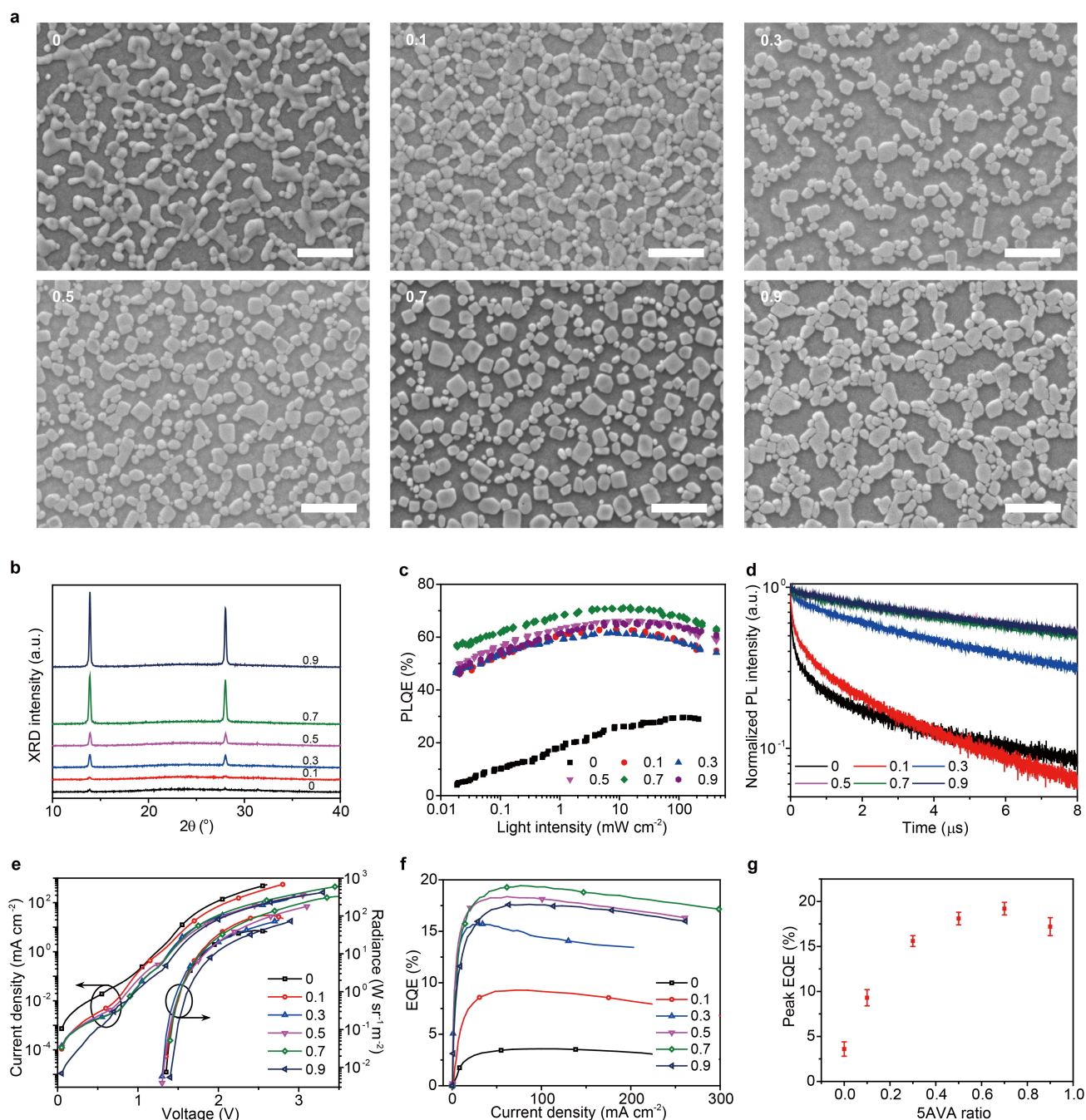
Extended Data Fig. 4 | Characterizations of perovskite films and LEDs with various 5AVA amounts. The ratio of 5AVA to FAI to PbI$_2$ is x/2.4/1, where x varies from 0 to 0.9. **a**, SEM images. The scale bars represent 1 μm. The value of x is given in the top left corner of each image. The reference FAPbI$_3$ perovskite film without 5AVA has low film coverage. Without 5AVA, the perovskites form discrete clusters with random shapes. After adding 5AVA, faceted perovskites with submicrometre structures gradually form. **b**, XRD spectra. The perovskite films show improved crystallinity with the addition of 5AVA. **c**, Excitation-intensity-dependent PLQE. After adding 5AVA, PLQEs were greatly enhanced, indicating reduced trap densities. **d**, Time-resolved PL decay transients

(carrier density 1.0×10^{13} cm^{-3}). There is a fast PL decay channel for the perovskite without 5AVA, indicating a high level of trap densities. This fast PL decay channel gradually disappears after adding 5AVA. **e**, Dependence of current density and radiance on the driving voltage. After adding 5AVA, the leakage current is reduced. **f**, EQE plotted against current density. **g**, Peak EQE plotted against 5AVA ratio. Error bars correspond to the standard deviation. After adding 5AVA, the peak EQE increases owing to reduced leakage current and enhanced PLQE. When the 5AVA ratio is increased to 0.9, the EQE decreases, owing to the inferior outcoupling efficiency that results from the more dispersed structural pattern.
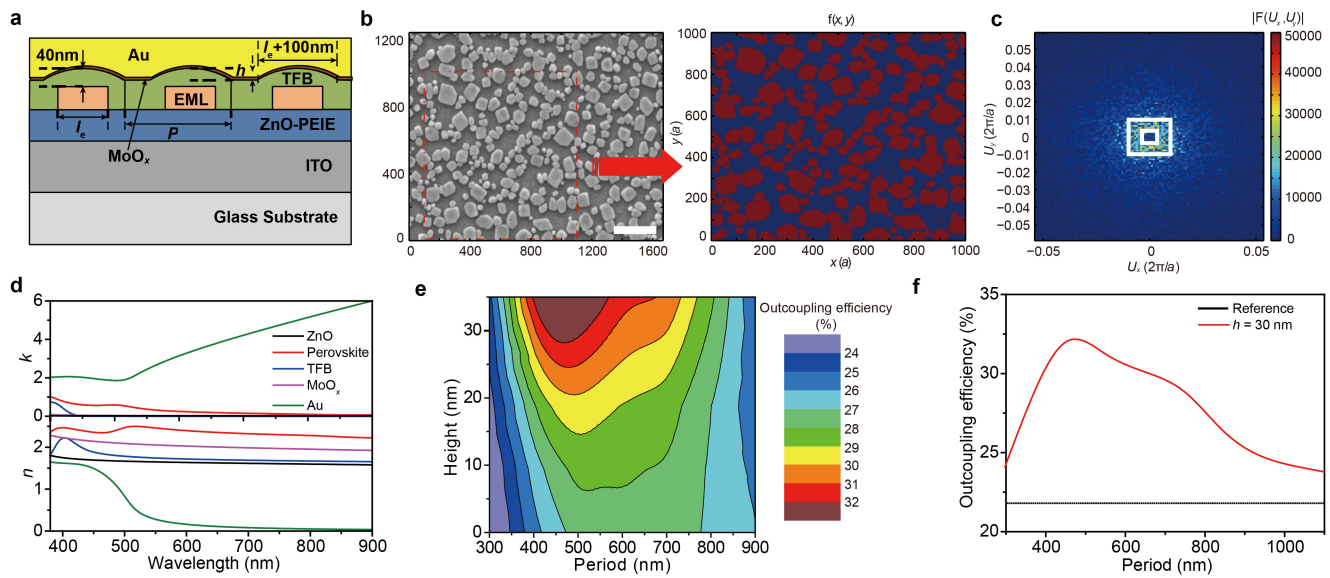
Extended Data Fig. 5 | Simulation of outcoupling efficiency. a, Device structure. A typical reference device consists of a metal layer (Au), a 7-nm-thick MoO_3 layer, a 40-nm-thick TFB layer, a 50-nm-thick emitting layer (EML), a 30-nm-thick layer of ZnO-PEIE, a 160-nm-thick ITO layer and a semi-infinite glass substrate. In our new device, the EML is replaced by a layer of perovskite squares distributed with a period P and a duty cycle l_e/P (where l_e is the length of the perovskite platelets, and $l_e/P = 50\%$). The height of the convex structure of TFB is denoted as h and the diameter is set to $l_e + 100$ nm. **b**, Discretized map of the perovskite layer. The scale bar represents 1 μm. x and y are the pixel numbers in units of pixel length a.

$f(x,y)$ is the discrete function. **c**, Module of spatial frequency spectrum. U_x and U_y are the spatial frequencies. **d**, Refractive indices of different layers in our perovskite LEDs. Optical constants (n, k) of the multilayers were determined using an ellipsometer. Here the optical constants of perovskite are from a continuous $FAPbI_3$ film, which are used in the simulation. **e**, EQE calculated as the period P and the convex height h. **f**, Calculated outcoupling efficiency as a function of period P with convex height $h = 30$ nm. The reference is a device made from continuous perovskite film. The simulation shows that the outcoupling efficiency can be more than 25% over a wide range of periods from 310 nm to 900 nm.
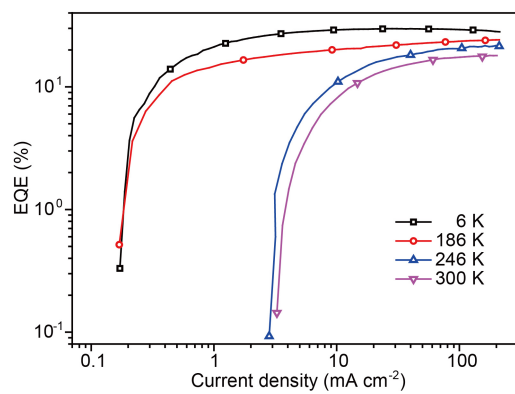
Extended Data Fig. 6 | EQE versus current density for our perovskite LED device at different temperatures. Measuring the device EQE at low temperatures minimizes nonradiative recombination so that the EQE reaches a value of 30% at 6 K.
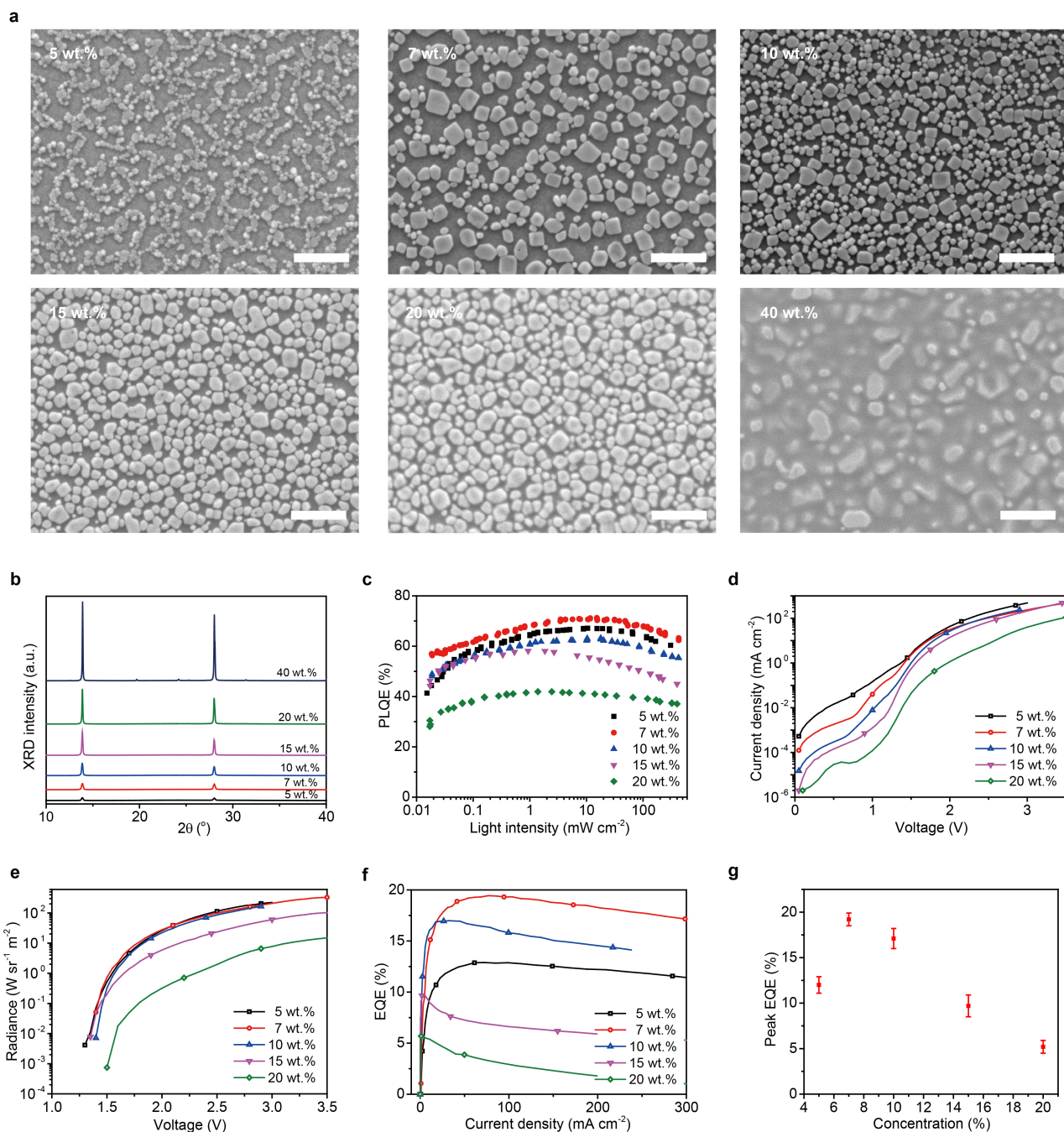
Extended Data Fig. 7 | Characterization of our perovskite films and LEDs at different precursor concentrations. a, SEM images. The scale bars represent 1 μm. As the precursor concentration increases (shown in the top left corner of each image), the size of the crystallites increases and the crystallites become more tightly packed. **b**, XRD spectra. **c**, Excitation-intensity-dependent PLQEs. The 7 wt.% film shows the highest PLQEs. **d**, Dependence of current density on driving voltage. The leakage currents of the devices decrease as the precursor solution becomes more concentrated. **e**, Dependence of radiance on the driving voltage. As the precursor concentration increases, the turn-on voltage increases and the radiance decreases, probably owing to the poor charge transport of thicker film. **f**, EQE plotted against current density. **g**, Peak EQE versus precursor concentration. Error bars correspond to the standard deviation. When the concentration exceeds 10 wt.% the EQE decreases, probably because of a reduced outcoupling-enhancement effect and poor charge transport.
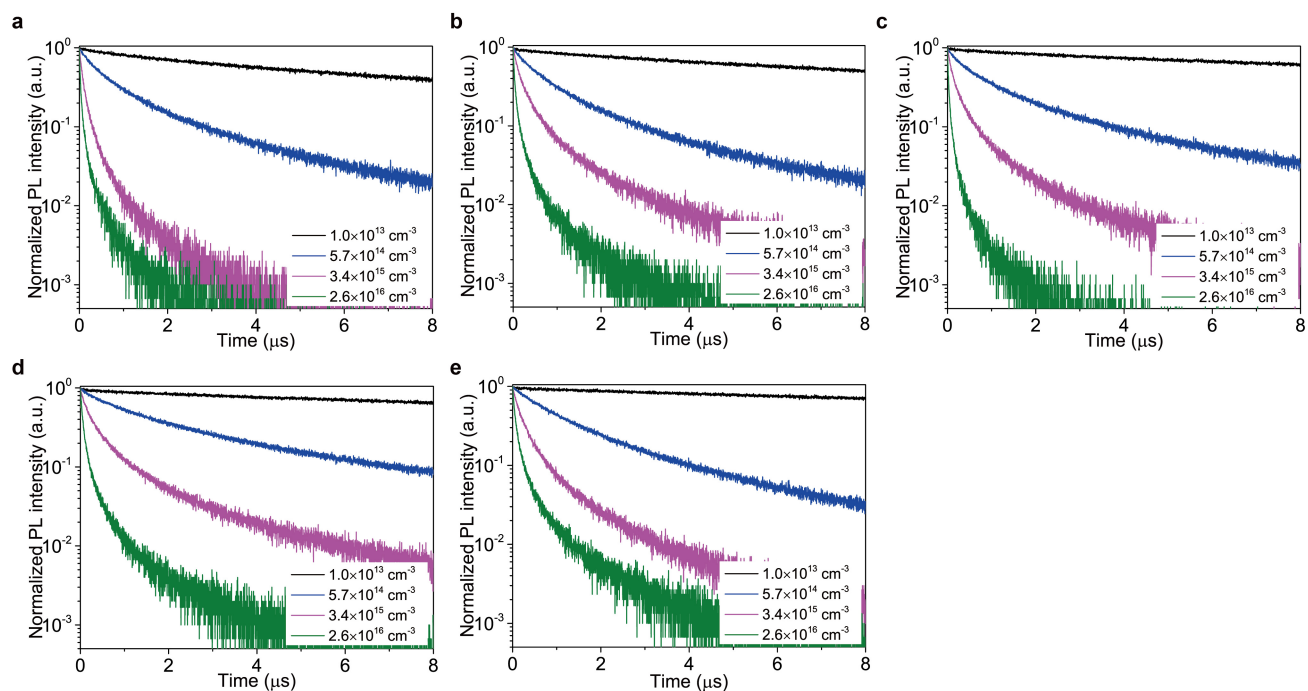
Extended Data Fig. 8 | Time-resolved photoluminescence decay transients of perovskites with different precursor concentrations. **a**, 5 wt.%. **b**, 7 wt.%. **c**, 10 wt.%. **d**, 15 wt.%. **e**, 20 wt.%. Charge carrier densities vary as indicated (black, blue, purple and green traces).
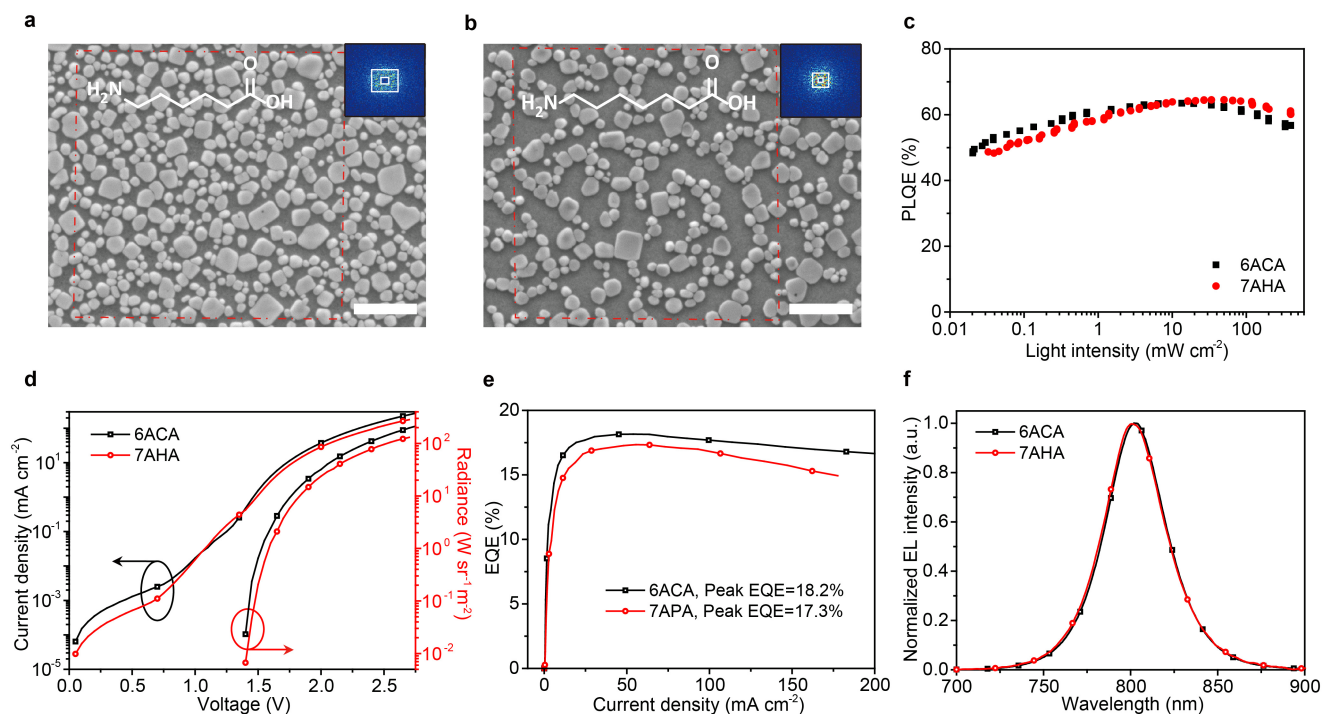
Extended Data Fig. 9 | Optoelectronic characteristics of perovskite LED devices fabricated with different amino acids in the precursor solution. a, SEM image of submicrometre-structured perovskites fabricated with 6ACA (chemical structure shown in white). The scale bar represents 1 μm. Inset, FFT pattern in a randomly selected region. The *P* range of 6ACA is 265–901 nm, yielding a calculated outcoupling efficiency of 28.9% ± 2.5%. **b**, SEM image of submicrometre-structured perovskites fabricated with 7AHA (chemical structure shown in white). The scale bar represents 1 μm. Inset, FFT pattern in a randomly selected region. The *P* range of 7AHA is 432–1,430 nm, yielding a calculated outcoupling efficiency of 26.4% ± 3.3%. **c**, Excitation-intensity-dependent PLQE. The perovskite films with 6ACA and 7AHA have similar PLQEs. **d**, Dependence of current density and radiance on the driving voltage. **e**, EQE versus current density. The 6ACA- and 7AHA-based devices reach peak EQEs of 18.2% and 17.3%, respectively. Given that the perovskite films based on 6ACA and 7AHA have similar PLQEs, the EQEs must be affected mainly by the different outcoupling efficiencies that result from the different periodicities of the submicrometre-scale structures. **f**, Electroluminescence spectra.

Extended Data Table 1 | Comparison of our device with reported high-performance organic LEDs

Device*	NIR		Red	Green	Blue
	Our LED	**OLED**[38]	**OLED**[39]	**OLED**[40]	**OLED**[41]
Peak EQE (%)	20.7	24	35.6	29.2	36.7
Current density (mA cm^{-2}) @ peak EQE	18	0.4[†]	0.7[†]	1[†]	0.1[†]
Photon flux ($\times 10^{20}$ m^{-2}s^{-1}) @ peak EQE	2.33	0.06[‡]	0.16[‡]	0.18[‡]	0.02[‡]
EQE (%) @ 100 mA cm^{-2}	19	-	-	19[†]	-
ECE (%) @ 100 mA cm^{-2}	12	-	-	5.6[‡]	-
EL peak (nm)	803	740	610	525	490[†]

Our perovskite LED device is compared with the organic LEDs (OLEDs) reported in refs [38–41].
*The table includes organic LEDs with horizontally orientated emitting dipoles, but without external optical outcoupling schemes (an example of an optical outcoupling scheme being a microlens with a glass substrate).
[†]These data were obtained from the figures in refs [38–41].
[‡]These data were estimated from the EQE, current density, voltage or photon energy at the electroluminescence peak.

Extended Data Table 2 | Comparison of devices measured in different laboratories

Device	Group	Peak EQE (%)[†]
PeLEDs[*]	Nanjing Tech University	15.2±0.3
	Cambridge University	15.3±0.5
	Zhejiang University	15.1±0.3

[*]The perovskite LEDs (PeLEDs) were fabricated in the same batch at Nanjing Tech University. Each set of devices without encapsulations was simultaneously measured in air until the Optoelectronics Group, Cambridge, received its samples. As the transfer time from Nanjing to Cambridge is about eight days, the devices suffer from modest degradations.
[†]The average peak EQE and standard deviation are from ten devices.